Three-body decay of the $3s\,^2A_1'(N=1, K=0)$ and $3d\,^2E''(N=1, G=0, R=1)$ Rydberg states of the triatomic hydrogen molecule H_3

U. Müller* and P. C. Cosby
Molecular Physics Laboratory, SRI International, Menlo Park, California 94025
(Received 28 December 1998)

The breakup of $n=3$ Rydberg states of the triatomic hydrogen molecule into three H($1s$) atoms was studied using SRI's fast neutral beam photofragment spectrometer. A beam of fast metastable H_3 $2p\,^2A_2''(N=K=0)$ molecules was generated by charge transfer of H_3^+ ions in Cs vapor. The metastable beam was crossed by an intracavity dye laser beam in order to selectively prepare the $3s\,^2A_1'(N=1,\ K=0)$ and $3d\,^2E''(N=1,\ G=0,\ R=1)$ states of H_3. Correlated fragment pairs were detected by a time- and position-sensitive detector. For both excited states, the two-body decay into $H+H_2$ fragment pairs as well as the three-body breakup into three correlated H($1s$) fragments are open channels. The two processes produce distinguishable events on the time- and position-sensitive detector. For three-body decay, only two of the three products are detected. An extensive model using physically reasonable assumptions was developed in order to explain the observed spectra and to gain insight into the kinematics of the three-body breakup. Branching ratios between three- and two-body decay are estimated for the breakup of the H_3 $3s\,^2A_1'(N=1,\ K=0)$ and $3d\,^2E''(N=1,\ G=0,\ R=1)$ states, and compared to results of a two-dimensional wave-packet calculation. [S1050-2947(99)10705-4]

PACS number(s): 33.80.Gj

I. INTRODUCTION

The H_3 molecule as the simplest neutral polyatomic molecule plays the role of a prototype for studies of molecular fragmentation processes. The electronically excited states can be best viewed as Rydberg states around a tightly bound H_3^+ ion core. The unbound ground-state potential-energy surface consists of two sheets which cross each other in a conical intersection at D_{3h} (equilateral) symmetry [1–5]. The lower sheet asymptotically correlates to $H+H_2(X\,^1\Sigma_g^+)$, whereas the upper sheet correlates to $H+H_2(b\,^3\Sigma_u^+)$, which leads to three-body decay into three hydrogen atoms [2]. For all H_3 Rydberg states the two-body decay into $H+H_2$, as well as the three-body decay into three H($1s$) atoms, are open fragmentation channels. A study of the decay processes of H_3 Rydberg states and the product state distributions of the fragments gives insight into the nonadiabatic coupling mechanisms between the ground and upper state potential-energy surfaces. The two-body breakup of H_3 $2s\,^2A_1'$, $3s\,^2A_1'$, and $3d\,^2E''$ molecules which were prepared in well-defined rotational and vibrational levels by laser excitation from the metastable $2p\,^2A_2''$ state has been investigated recently by Müller and Cosby [6]. Information on the three-body breakup of these states remains relatively scarce. There is, however, direct information that has been obtained from the study of dissociative charge transfer of H_3^+ and D_3^+, and from the dissociative recombination of H_3^+.

The formation of hydrogen atoms upon two- and three-body decay of the H_3 $2s\,^2A_1'$ and $2p\,^2A_2''$ states was studied by Peterson *et al.* [7]. In their experiment, H_3 molecules were generated by charge transfer of H_3^+ in Cs. Hydrogen atoms from the H_3 breakup were detected as H^- atoms formed by subsequent electron attachment in Cs, and subjected to kinetic-energy analysis which found two broad maxima in the center-of-mass (c.m.) kinetic energy release distribution. Associating the lower- and higher-energy maxima with the three- and two-body dissociation products, respectively, allowed the branching ratio of these channels to be estimated. The dependence of this ratio on the rovibrational energy of the H_3 parent state was studied by changing the temperature of the H_3^+ precursor using different types of ion sources. Isotope effects were studied as well. Three- to two-body branching ratios of 0.23 and 0.35 were found for H_3 and D_3, respectively, with a rotationally cold hollow cathode discharge source. Ratios of 0.65 and 0.57 for H_3 and D_3, respectively, were observed with rotationally-hot parent ions produced by a Colutron-type source. Their results refer to an unknown distribution of electronic states in the H_3; most likely these are the $n=2$ Rydberg states, which should be preferentially formed by near-resonant change exchange in the H_3^+/Cs neutralization.

Mitchell and co-workers [8,9] studied the dissociative recombination of H_3^+ with free electrons in a merged-beam experiment. This process is considered to involve high-n Rydberg states of H_3. The two- and three-body dissociation products were distinguished by their relative attenuation with a semitransparent grid. The cross section for three-body fragmentation into H+H+H was found to be about a factor of 1.3 higher than that of the two-body breakup into $H+H_2$. Datz *et al.* [10] recently performed a merged-beam experiment using the electron cooler at CRYRING, distinguishing the three- and two-body dissociation products by their relative transmissions through a semitransparent grid. The ratio of about 3 between the cross sections for three- and two-body breakup was observed for dissociative recombination at electron energies up to about 500 meV [10]. At higher electron energies, this ratio exhibits a strong dependence on electron energy.

*Present address: Fakultät für Physik, Universität Freiburg, Hermann-Herder Str. 3, D-79104 Freiburg, Germany.

A theoretical investigation of H_3 dissociation was performed by Orel and Kulander [11]. A two-dimensional wave-packet treatment was applied, and the geometry was restricted to that of an isosceles triangle (C_{2v}). For several states of the H_3 Rydberg series, the H_2 final state vibrational populations and three-/two-body branching ratios were calculated. For the fragmentation of the vibrationless $2s\ ^2A_1'$ state, a three-/two-body branching ratio of 0.64 was found. The ratios generally increase with a higher vibrational excitation of the initial state. In order to take the influence of the initial state electronic wave function into account, Krause *et al.* [2] included nonadiabatic coupling matrix elements into the wave-packet treatment and reported product state distributions and branching ratios for the $3s\ ^2A_1'$ initial state.

In the present work, we have used fast beam photofragment spectrometry [12] to investigate the fragmentation of the (optically prepared) $3s\ ^2A_1'(N=1,\ K=0)$ and $3d\ ^2E''(N=1,\ G=0,\ R=1)$ states of the H_3 molecule. Although the spectrometer can only detect two fragments in coincidence, the correlation in the spatial and temporal separations of the detected fragments from a subset of the dissociation products can be clearly attributed to the three-body breakup of H_3 into H+H+H atoms. A numerical model which applies physically reasonable assumptions about the symmetry of the fragmentation pattern and a Monte Carlo simulation of the detector response are used to obtain insight into the kinematics of the three-body breakup and to estimate the two-/three-body branching in the predissociation of the ground vibrational levels in the $3s\ ^2A_1'(N=1,\ K=0)$ and $3d\ ^2E''(N=1,\ G=0,\ R=1)$ states.

II. EXPERIMENT

The experimental setup is similar to that reported in previous publications from this laboratory [6,12], and will be discussed here only briefly. Rotationally and vibrationally cold H_3^+ ions were created in a hollow cathode discharge source. The ions were accelerated to a selected energy in the range of 3–6 keV, and mass selected by a magnetic sector. The H_3^+ beam then enters an oven containing cesium vapor and a fraction (<10%) is neutralized by charge transfer into $n=2-3$ Rydberg states of H_3. Unneutralized ions passing through the cell are removed from the beam by a weak electric deflection field. Nearly all of the Rydberg states rapidly predissociate except for the single H_3 quantum state $2p\ ^2A_2''(N=K=0)$, which is sufficiently long lived (640 ns [13]) to be collimated into a molecular beam and probed by laser excitation. Separation of the metastable H_3 beam from the dissociative charge-transfer products is accomplished by a narrow (500 μm) slit located 54 cm downstream from the charge-transfer cell. All neutrals passing through this slit are intercepted by a 1.2-mm-wide beam flag positioned 10 cm downstream from the slit. Fragments from neutral molecules dissociating within this 10-cm interval, which are produced with sufficient velocity transverse to the beam direction to escape collection by the beam flag, travel an additional 100 cm to the detector.

Optical transitions into the $3s$ and $3d$ levels of the H_3 molecule were pumped using a *cw* dye laser (Rhodamine 6G)–argon-ion laser combination. The dye laser was operated with an extended cavity whose ~2-mm-diameter beam intersected the H_3 beam approximately 2 mm downstream from the slit, with the electric vector of the linearly polarized laser perpendicular to the velocity of the H_3 beam. An angle-tuned, 0.1-mm-thick solid etalon was also included in the laser cavity, and narrowed the laser linewidth to $<0.1\ \mathrm{cm}^{-1}$. The typical intracavity laser power was ~25 W. A fraction of the laser light was coupled into a wavemeter (Burleigh, Wavemeter jr) for wavelength calibration.

In the present investigation, we used SRI's time- and position-sensitive detector which has been described in detail [12,14]. Correlated photofragment pairs produced by the dissociation of individual molecules are detected in coincidence. The detector consists of two sensitive sections located on opposite sides of the neutral beam axis which measure the radial distances R_1 and R_2 of fragment impacts relative to the detector center and the difference in the fragment arrival times ($\Delta t = t_2 - t_1$). A laboratory computer was used to perform on-line data evaluation, reducing the observed values of R_1, R_2, and Δt to the quantities

$$Z \equiv \frac{R_1}{R_2}\left(1 - \frac{v_0 \Delta t}{L_0}\right) \tag{1}$$

and

$$W = E_0\left(\frac{m_1 m_2}{M^2}\right)\left(\frac{R^2 + (v_0 \Delta t)^2}{L_0^2}\right)\left[1 - 2\left(\frac{v_0 \Delta t}{L_0}\right)\frac{|m_2 - m_1|}{M}\right], \tag{2}$$

which are accumulated as two histograms for a series of dissociation events. In these equations, $R = R_1 + R_2$ is the total radial separation of the fragments, E_0 is the primary beam energy, $v_0 = \sqrt{2E_0/M}$ is the velocity of the c.m., and L_0 is the distance between the interaction region and the detector. These equations describe the two-body breakup of a parent molecule of known mass M into fragments with masses m_1 and m_2. In this case, the distance ratio Z reflects the mass ratio of the fragments, m_2/m_1, and W corresponds to the kinetic energy released in the dissociation.

For the case of a three-body dissociation, each side of the detector must be hit by at least one of the three fragments, in order to generate a coincident event. Since the active area of the detector consists of two 36° sectors positioned above and below the neutral beam, it is rare that more than two of the three H-atom fragments will strike an active area. Nevertheless, when two of the three fragments hit on one side of the detector, the double hit leads to a distortion of the time and position measurement: the time information is determined by the first arriving particle and the position information corresponds to an average between the locations of both fragment impacts. For the three-body dissociation products, the quantity Z derived from Eq. (1) retains much of its physical significance and can be used to distinguish between the two-body dissociation channel $H_3 \rightarrow H + H_2$ ($Z = 0.5$ or 2) and three-body dissociation channel $H_3 \rightarrow H + H + H$ ($Z \neq 0.5$ or 2). However, the value of W derived from Eq. (2) has no exact physical significance for the case of three-body dissociation products. Rather, its calculation in Eq. (2) provides only a convenient method for recording a histogram summary of the correlation between R and Δt in several hundred thousand detected coincidences. An approximate relationship

between the calculated value of W and the translational energy release of the dissociation can be achieved if the dissociation is viewed as occurring in two sequential steps:

$$H_3 \rightarrow H + H_2^*,$$

$$H_2^* \rightarrow H + H,$$

thus assigning $M = M(H_2^*)$, $m_1 = m_2 = m(H)$, and $E_0 = E_0(H_2^*) = \frac{2}{3}E_0(H_3)$ in Eqs. (1) and (2). Such an association, however, is not important for an analysis of the detected coincidences, which is based on a Monte Carlo simulation of the three-body dissociation dynamics, as discussed in Sec. III (see Fig. 1). Rather, it is only important that the values of m_1, m_2, M, and E_0 of Eqs. (1) and (2) used in the simulation be the same as those used for the data acquisition.

III. RESULTS AND ANALYSIS

A. Evidence of the three-body decay from experimental data

In Fig. 2, multichannel spectra of the distance ratio Z are presented resulting from the metastable decay of the H_3 $2p\,^2A_2''(N=K=0)$ state [spectrum (a)] and from photofragmentation of the vibrationless $3d\,^2E''(N=1, G=0, R=1)$ and $3s\,^2A_1'(N=1, K=0)$ states [spectra (b) and (c), respectively]. The strong peaks at $Z=0.5$ and 2 are readily assigned to decay processes leading to $H+H_2$ fragment pairs with $m_1=1$ and $m_2=2$, or vice versa. In the previous investigation [6] of the two-body breakup, the value of Z was used to impose a restriction on the events accepted for the collection of kinetic-energy release spectra. In addition to the strong peaks in Fig. 2, a continuous contribution extending from $Z=0.25$ to 2.5 peaking around $Z=1.0$ is observed. This contribution is strongest in the case of the $3s$ level [spectrum (c)], weaker in the case of the $3d$ level [spectrum (b)], and barely noticeable for the metastable decay [spectrum (a)]. The fragmentation of a diatomic molecule (e.g., H_2) can be excluded as the precursor of the feature, since it would result in a discrete peak at $Z=1$. The broad distribution can be understood to arise from a breakup of H_3 into three $H(1s)$ atoms. The kinetic energy can be distributed in many different ways among the three fragments, which leads to a large variety of possible fragmentation geometries. One of the three fragments either remains unobserved or leads to a double hit on one side of the detector. In order to produce sharp structures in the Z spectrum, momentum conservation must be valid for the two observed particles. In the case of a three-body breakup, the momentum of the third unobserved particle remains unknown which leads to a broad distribution in the Z spectrum.

In the following measurement, events with a distance ratio Z outside of the interval 0.7 to 1.4 were ignored. In this way, only those events which lead to the maximum of the continuous feature in the distance-ratio spectrum are collected, and events from two-body decay are effectively suppressed. The resulting spectrum of the apparent kinetic-energy release W following decay of the H_3 $3s\,^2A_1'(N=1, K=0)$ ν_0 state is presented in the lower part of Fig. 3 as spectrum (c). The arithmetic of the on-line data evaluation was adapted to the fragmentation of H_2 molecules having the same velocity as the 6-keV H_3^+ primary beam [$m_1=m_2=1$, $M=2m_1$, $E_0=4$ keV in Eqs. (1) and (2)]. The spectrum is monotonically rising from low kinetic-energy release W to a double peak at 2.7 and 3.1 eV followed by a sharp cutoff at about 3.2 eV. Since the laser was chopped and the laser-off spectrum was subtracted, the result is not affected by metastable decay.

It should be noted that the spectrum presented in Fig. 3 has no similarity to the kinetic-energy release spectrum observed for the two-body fragmentation channel of the $3s\,^2A_1'(N=1, K=0)$ ν_0 state (see Fig. 11 of Ref. [6]). This shows that the two-body fragmentation channel was effectively suppressed by restricting the allowed Z ratio to the interval 0.7–1.4.

In order to check for the contributions of false coincidences to the spectrum in Fig. 3, we performed a Monte Carlo simulation of the W spectrum, assuming realistic distributions of events on both detector plates and on the time scale. The shape of the false coincidence spectrum has no similarity with the W spectrum observed in Fig. 3. It extends to far higher values of W, and does not show the cutoff at 3.2 eV. This reflects the absence of correlation between R and Δt for such events. On the other hand, the simulation of false coincidences yields a Z spectrum, peaking at unity, which cannot in itself be distinguished from that attributable to three-body dissociation. We estimate that false coincidences constitute less than 3% of the events in the spectrum in Fig. 3.

B. General model of three-body breakup

The system of three fragments has far more degrees of freedom than the number of coordinates which can be measured by the time-and position-sensitive detector. We developed a model of the three-body fragmentation which allows us to reduce the number of degrees of freedom by reasonable assumptions in order to understand the shape of the observed spectra and to extract physically meaningful information.

The kinematics of the breakup process of a molecule with mass M and laboratory velocity vector $\mathbf{v}_0$ into three fragments with masses m_i and laboratory velocity vectors $\mathbf{v}_i$ is governed by the conservation of momentum and mass:

$$\sum_{i=1}^{3} m_i \mathbf{v}_i = M \mathbf{v}_0, \tag{3}$$

$$\sum_{i=1}^{3} m_i = M. \tag{4}$$

For equal masses m_i, as is appropriate for the case of H_3, the relations between the fragment velocities $\mathbf{u}_i = \mathbf{v}_i - \mathbf{v}_0$ in the center-of-mass frame simplify to

$$\sum_{i=1}^{3} \mathbf{u}_i = \mathbf{0}, \tag{5}$$

The velocity vectors $\mathbf{u}_i$ define a plane in space and have six independent components.

We can always find a coordinate system (x',y',z') in which the fragment velocity vectors can be expressed by

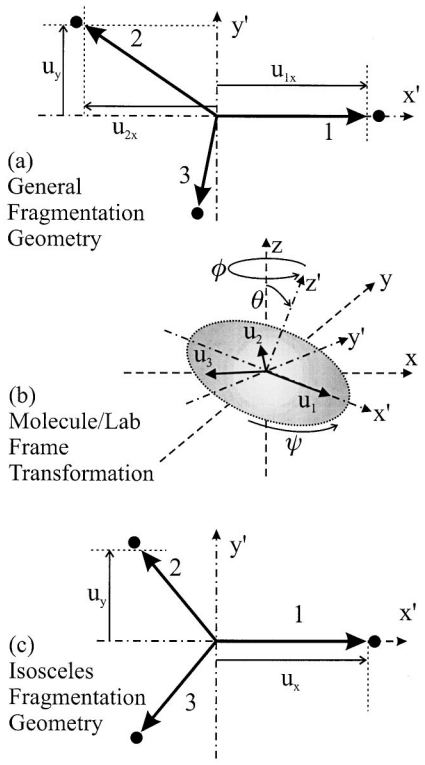

FIG. 1. Schematic diagrams of the coordinate frames used in the kinematic model for the dissociation of H_3 into H+H+H. (a) Components of the H-atom velocity vectors within the x',y' plane of the molecule. (b) Transformation of the (x',y',z') coordinates of the fragments into (x,y,z) coordinates of the laboratory frame. (c) Components of the H-atom velocity vectors within the x',y' plane of the molecule for the restricted isosceles model of the H_3 dissociation.

$$\mathbf{u}_1'=(u_{1x},0,0),$$

$$\mathbf{u}_2'=(u_{2x},u_y,0), \tag{6}$$

$$\mathbf{u}_3'=(-(u_{1x}+u_{2x})-u_y,0),$$

which is shown schematically in Fig. 1(a). This new coordinate system is rotated with respect to the laboratory-fixed (x,y,z) system by the Eulerian angles (θ,ϕ,Ψ) as shown in Fig. 1(b). The angles (θ,ϕ) define the orientation of the z' axis in the laboratory frame, and angle Ψ defines rotation within the (x',y') plane. The vectors $\mathbf{u}_i'$ are contained in the (x',y') plane, and $\mathbf{u}_1'$ is oriented parallel to the x' axis. We take the z' axis to coincide with the top axis of the parent H_3 molecule, and assume the fragment ejection pattern to be symmetric with respect to rotation about this axis. Therefore, distributions of ϕ and Ψ are assumed to be random between 0 and 2π. Within the laboratory coordinate frame, the axes are chosen such that the H_3 beam propagates along the x axis and the laser polarization vector is along the z axis. The detector lies in the y,z plane with its active regions extending to $\pm z$.

The angular distribution of the axis of a symmetric top following absorption of linearly polarized light is well known [15]. In the case of the $3s\ ^2A_1'(N=1,K=0) \leftarrow 2p\ ^2A_2''(N=K=0)$ transition, the change of dipole moment is parallel to the figure axis (parallel transition) which results in a $\cos^2\theta$ distribution of the molecular top axis with respect to the laser polarization, which is described by an asymmetry parameter $\beta=2$. In the case of two-body breakup, the angle of fragment ejection was observed to follow a $\sin^2\theta$ distribution with respect to the laser polarization [6], which justifies the assumption that the fragments are ejected perpendicular to the molecular top axis. In the case of the $3d\ ^2E''(N=1,\ G=0,\ R=1) \leftarrow 2p\ ^2A_2''(N=K=0)$ transition, we expect an alignment of the molecular top axis described by $\beta=0.2$, which should yield a near-isotropic distribution in the fragments, as has been observed for the two-body dissociation channel [6,16,17].

The degrees of freedom of the system are now reduced to the three components of the vectors $\mathbf{u}_1'$. These could be parametrized by Jacobi coordinates which are generally used in theoretical investigations [2,18]. We prefer instead to introduce the total kinetic energy W_0 released to the fragments by

$$W_0=\sum_{i=1}^{3} \tfrac{1}{2} m\mathbf{u}_i^2, \tag{7}$$

since optical preparation of the H_3 allows this to be single valued and well defined. The energies of the H_3 $3s\ ^2A_1'(N=1,\ K=0)$ ν_0 and the $3d\ ^2E''(N=1,\ G=0,\ R=1)$ ν_0 states above the $H+H_2(v=0,J=0)$ dissociation limit are well known [19]. Using these and the dissociation energy of H_2, we find the energy of the H_3 $3s\ ^2A_1'(N=1,\ K=0)$ ν_0 and the $3d\ ^2E''(N=1,\ G=0,\ R=1)$ ν_0 states to be 3.155 and 3.230 eV, respectively, above the three-body dissociation limit. Since these energies must be completely released as kinetic energy W_0 of the fragments by predissociation, the system has only two degrees of freedom remaining.

We will consider an unrestricted treatment of these two degrees of freedom in three-body dissociation further in Sec. III D. However, it is instructive to first view the dissociation within the framework of a restricted dissociation geometry in which the fragments have only one degree of freedom.

C. Isosceles fragmentation geometry

In a first attempt to understand the shape of the experimentally observed spectra, it is instructive to restrict the fragmentation geometry to that of an isosceles triangle. This restriction also facilitates a comparison between the experimental results and the *ab initio* calculations of Orel and Kulander [11], who used a two-dimensional wave-packet description of H_3 dissociation.

In the isosceles geometry, shown schematically in Fig. 1(c), the x and y components of the fragment velocity vectors $\mathbf{u}_i'$,

$$\mathbf{u}_1'=(u_x,0,0),$$

$$\mathbf{u}_2'=(-0.5u_x,u_y,0), \tag{8}$$

$$\mathbf{u}_3'=(-0.5u_x,-u_y,0),$$

can be calculated from the total kinetic-energy release W_0 and the value of a parameter p,

$$u_x = p u_y , \tag{9}$$

$$u_y = \left(\frac{2W_0}{m(2+3p^2/2)} \right)^{1/2} . \tag{10}$$

Since W_0 is known from the discrete energy of the molecular state, the fragmentation geometry is solely determined by the parameter p, which can assume values in the range $0 \leqslant p \leqslant \infty$. The relative partitioning of the fragment velocities is shown schematically for several values of p on this interval by the diagrams in the top portion of Fig. 3.

For the total kinetic-energy release of $W_0 = 3.155$ eV, a $\beta = 2$ alignment of the z' axis, and specific values of the parameter p, we performed a Monte Carlo simulation of the detector response. Sets of fragment velocity vectors $\mathbf{u}_i$ were generated and transformed into fragment trajectories in the laboratory frame. Taking into account the geometry of the apparatus and the properties of the detector electronics, as had been established in our earlier study [6] of H_3, the ability of each trajectory to strike an active region of the detector is determined, as is its radial separation and arrival time. For the case of two fragments striking one side of the detector, which turns out to be a comparatively rare event, the time information is determined by the first arriving particle and the mean value between the locations of the two impacts is taken as the radial position information. The calculated values of R and Δt for each detectable trajectory are accumulated as histograms of apparent Z and W with Eqs. (1) and (2), using the mass, distance, and energy parameters that had been employed in the experimental data acquisition. Typically $10^5 - 10^6$ trajectories are calculated to generate statistically significant Z and W spectra for each value of the parameter p.

The detector collection efficiency for three-body events calculated from the Monte Carlo simulation as a function of the parameter p is shown by the dashed curve (a) in the top part of Fig. 3. The maximum in this normalized curve occurs for values of p near zero, and corresponds to an absolute efficiency of 8.3%. This maximum can be understood since $p = 0$ represents a configuration for which the detector is optimized. Other efficiently detected fragmentation geometries are produced as $p \rightarrow \infty$, but these correspond closely to two-body dissociation and yield values for Z outside the collected interval of $0.7 \leqslant Z \leqslant 1.4$. For other values of p, it is more difficult for at least two of the three fragments to fall onto active areas of the detector. The collection efficiency is poorest for a partitioning of the fragment velocities in an equilateral geometry ($p = 2/\sqrt{3}$).

The apparent kinetic-energy release spectra calculated by the Monte Carlo simulation procedure for the values 0, 0.5, 1.15, and 2.0 of the parameter p are included in the lower part of Fig. 3. For $p = 0$, we find a huge, narrow peak at $W = W_0 = 3.155$ eV, which must be scaled down by a factor of 20 to be included in the plot. In this fragmentation geometry, the total available energy is released in the two terminal hydrogen atoms with the central atom staying at rest in the c.m. frame. This situation corresponds to the breakup of a H_2 molecule traveling with the H_3 parent's velocity in the laboratory frame and a kinetic-energy release of W_0, producing the highest possible values of apparent kinetic-energy release and detector collection efficiency. The maximum at 3.1 eV in the measured spectrum [(c) in Fig. 3] and the subsequent cutoff at higher values of W can be understood to result from fragmentation processes with p close to zero, which are detected most effectively.

With increasing values of p, more energy goes into the third, unobserved fragment and the apparent kinetic-energy release is lowered. At $p = 2/\sqrt{3} \cong 1.15$, the fragmentation geometry is equilateral. This yields a double-peaked feature centered around 1.6 eV in the apparent kinetic-energy release spectrum, which is half of the total available energy. The unobserved third particle may be ejected behind or ahead of the center of mass, respectively, producing the higher or lower effective energy release contributions in the pair. These two contributions are relatively distinct, since ejection of the unobserved third particle orthogonal to the center-of-mass velocity makes it difficult for the remaining two atoms to fall onto an active region of the detector. This same pair of contributions to the apparent energy release spectrum also occurs at other finite values of p. In addition, these triangular configurations produce two velocity classes in the fragment pairs which appear at different effective kinetic-energy releases in the spectra.

The apparent kinetic-energy spectra calculated for discrete values of p can be used as basis functions to fit the measured spectrum, curve (c) in Fig. 3, resulting from decay of the H_3 $3s\,{}^2A_1'(N=1, K=0)$ ν_0 state. The result of this fit, shown as spectrum (d) in Fig. 3, closely resembles the measured spectrum, apart from small, but significant, deviations near $W = 1.2$ and 2.2 eV, where the synthetic spectrum is more intense than the measured spectrum. The distribution of the parameter p determined by the fit is shown by curve (b) in the upper part of Fig. 3 as the diamonds connected by a solid line. This p distribution was also used to calculate a synthetic distribution of fragment distance ratios Z using Eq. (1). The result (not shown) explains the broad distribution in the experimental spectrum in Fig. 2 peaking at $Z = 1$. The ability of the p distribution to reproduce both the distance-time correlation embodied in the apparent W spectrum and the distance correlation embodied in the apparent Z spectrum gives some confidence as to its uniqueness.

The discrepancies between the experimental curve and the fit at $W = 1.2$ and 2.2 eV (the lower part of Fig. 3) indicate that our initial model used to calculate the basis functions is too restrictive. The assumptions of the model overemphasize the isosceles fragmentation geometry which is only a minor fraction of the whole range of geometries.

D. Full parametrization of the fragmentation geometry

A more general parameterization of the fragmentation geometry allows us to describe all possible configurations for axial ejection of three H atoms in the dissociation of a discrete H_3 state. In this model, two parameters a and b describe partitioning of the total kinetic-energy release W_0 in the c.m. frame among the fragments:

$$\tfrac{1}{2} m \mathbf{u}_1^2 = a W_0 , \quad \tfrac{1}{2} m \mathbf{u}_2^2 = b W_0 , \quad \tfrac{1}{2} m \mathbf{u}_3^2 = (1-a-b) W_0 , \tag{11}$$

where m is the mass of the fragment. In order to retain a unique correspondence between the parameters and the fragmentation geometry, we adopt the convention

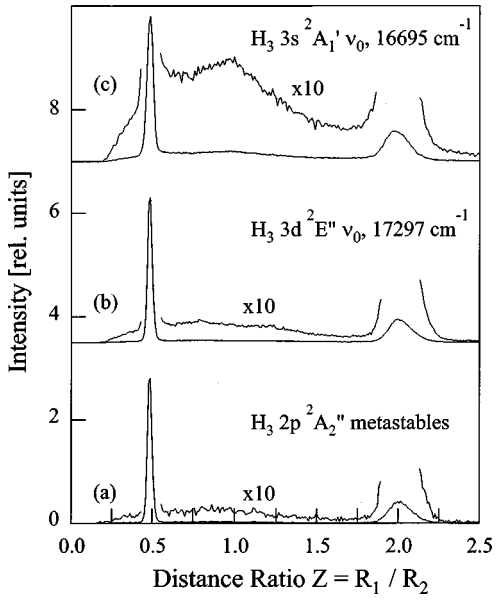

FIG. 2. Spectra of the distance ratio Z following fragmentation of the (a) $2p\ ^2A_2''(N=K=0)$, (b) $3d\ ^2E''(N=1,\ G=0,\ R=1)$, and (c) $3s\ ^2A_1'(N=1,\ K=0)$ states of the H_3 molecule. The strong peaks at 0.5 and 2.0 in each spectrum are due to two-body dissociation into $H+H_2$ fragment pairs. These discrete features are superimposed on a continuous distribution extending from $Z=0.25$ to 2.5, with a maximum at $Z=1.0$. The continuous features, which are more clearly visible in the spectra amplified by a factor of 10, are attributed to the three-body decay of H_3 into H+H+H fragments. This contribution is strongest in the case of the $3s\ ^2A_1'$ level.

$$a \leqslant b \leqslant 1-a-b, \tag{12}$$

which orders the individual fragments according to the magnitude of their velocities. Additionally, we require that particle 1 be located on the x' axis of the rotated coordinate system. From the values of parameters a and b, the mass m, and the kinetic-energy release W_0, the velocity components u_{1x}, u_{2x}, and u_y in Eq. (6) can be calculated:

$$u_{1x}=u_0\sqrt{a},$$

$$u_{2x}=u_0\frac{1/2-a-b}{\sqrt{a}}, \tag{13}$$

$$u_y=u_0\left(b-\frac{(1/2-a-b)^2}{a}\right)^{1/2},$$

where $u_0=\sqrt{2W_0/m}$. For the particular case of $a=0$, Eqs. (13) reduce to $u_{1x}=u_{2x}=0$ and $u_y=\sqrt{W_0/m}$.

With these conventions, parameter a can assume values within the range

$$0 \leqslant a \leqslant 1/3. \tag{14}$$

Energy and momentum conservation constrain parameter b to the range of values defined by

$$\tfrac{1}{2}(1-a) \geqslant b \geqslant \tfrac{1}{2}(1-a-\sqrt{2a-3a^2}) \tag{15}$$

or

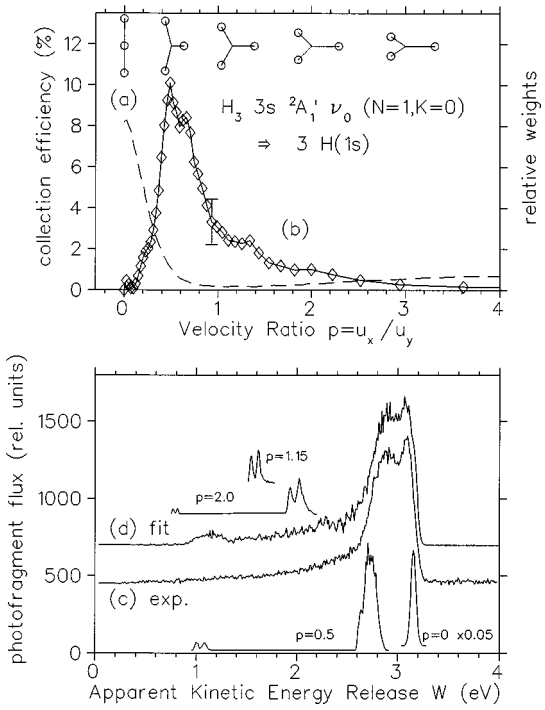

FIG. 3. Upper: Curve (*a*) (dashed line): relative apparatus collection efficiency (percent) as a function of parameter p. Curve (*b*) (diamonds): distribution of the parameter p which was used to generate the fitted spectrum (*d*). Schematic diagrams for the relative velocities of the three hydrogen atoms that correspond to several values of p are included along the top portion of this figure. Lower: Apparent kinetic-energy release following three-body fragmentation of the H_3 $3s\ ^2A_1'(N=1,\ K=0)$ ν_0 level. Spectrum (*c*) is the experimental histogram summarizing the spatial and temporal separations of the correlated three-body fragments. Spectrum (*d*) is a fit to the experimental spectrum by a weighted sum of basis functions. A model of the fragmentation process is assumed that restricts the geometry of the fragment velocity vectors to that of an isosceles triangle, with the parameter p describing the ratio between the velocity components $p=u_x/u_y$. Representative basis functions (apparent kinetic-energy release spectra) for $p=0$, 0.5, 1.15, and 2.0, calculated by a Monte Carlo simulation of the detector response, are included in the plot.

$$b \geqslant a, \tag{16}$$

whichever is more restrictive. In Fig. 4 we try to illustrate the relationship between the values of the parameters a and b and the fragmentation geometry. The kinematically allowed range of these parameters is represented by the area subtended by the dashed lines in this figure. Note that the isosceles geometry used for the restricted model corresponds only to the two straight line segments in this diagram, $a=b$ and $b=(1-a)/2$, showing how serious that restriction actually is. On the other hand, the experimental data are not sufficient to determine both independent parameters a and b simultaneously in an unrestricted fit to the experimental energy release spectrum. Therefore, we introduce a compromise into the unrestricted model by assuming parameter b to be uniformly distributed over its kinematically allowed range. In making this assumption, we lose the ability to determine the actual distribution in b and potentially introduce a systematic error by requiring its distribution to be uniform,

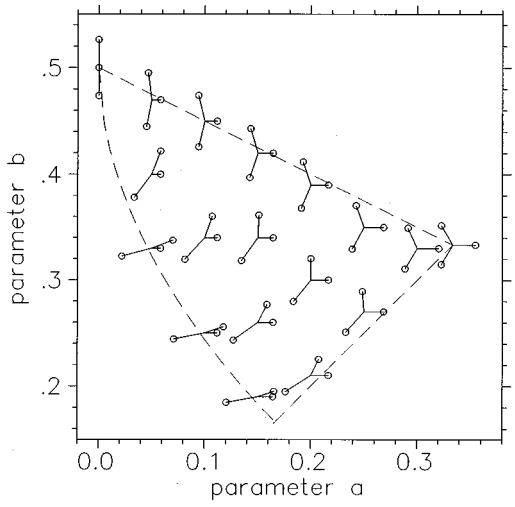

FIG. 4. Geometries of the fragment velocity vectors in a model that parametrizes the unrestricted sharing of total kinetic energy W_0 among the three fragments (see text). In these drawings, the velocity of the slowest fragment is directed along the abscissa and the origin of the three vectors defines the relevant values of *a* and *b*. For conservation of energy and momentum in the dissociation, the values of parameters *a* and *b* must fall within the area bounded by the dashed lines. In the isosceles model, *a* and *b* would be restricted to only those values that fall on the dashed straight lines at the top and right in this figure.

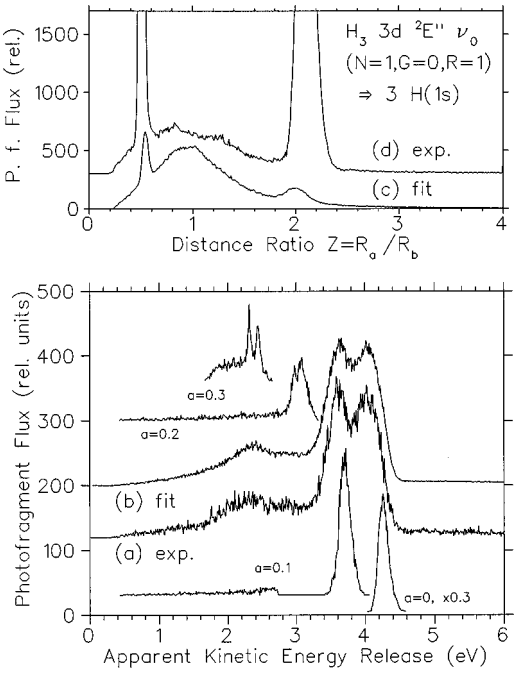

FIG. 5. Lower: Spectrum (*a*) apparent kinetic-energy release following three-body fragmentation of the H_3 $3s\,^2A_1'(N=1, K=0)$ initial state. Spectrum (*b*) is a fit to the experimental spectrum by a weighted sum of basis functions. The basis functions were calculated by a Monte Carlo simulation of the detector response using a model which parametrizes the sharing of the total kinetic energy between the fragments (cf. Fig. 4). For a fixed value of parameter *a*, the parameter *b* was distributed randomly in the kinematically allowed range. Basis functions (apparent kinetic-energy release distributions) for representative values of *a* ($a=0$, 0.1, 0.2, and 0.3) are included in the figure. Upper: Spectrum (*c*): simulation of the apparent *Z*-ratio spectrum using the parameter *a* distribution established for spectrum (*b*). Spectrum (*d*): experimental *Z*-ratio spectrum.

but at least the entire range of allowed configurations (see Fig. 4) is probed by the model.

Apparent kinetic-energy release spectra were calculated for discrete values of parameter *a* between 0 and $\frac{1}{3}$ by the Monte-Carlo simulation for use as basis functions to fit the experimental spectrum. We first consider the predissociation of the H_3 $3s\,^2A_1'(N=1, K=0)$ ν_0 state prepared with an optical alignment of the molecular top axis described by the asymmetry parameter $\beta=2$, with the plane of fragment ejection perpendicular to this axis. As previously noted, the experimental spectrum, shown again as spectrum (*a*) in Fig. 5, was accumulated using the set of parameter values ($m_1=m_2=1$, $M=2m_1$, $E_0=4$ keV) in Eq. (2). The calculated apparent kinetic-energy release distributions for the representative cases of $a=0$, 0.1, 0.2, and 0.3 are shown in Fig. 5 for reference. It is noted that these basis functions exhibit a less distinct structure than those derived from the isosceles model (see Fig. 3), due to averaging over the kinematically allowed range of the parameter *b*. Spectrum (*b*) in Fig. 5 is the result of fitting the experimental spectrum using a weighted sum of the basis functions. The fit is in excellent agreement with the experimental *W* spectrum [spectrum (*a*) in Fig. 5], eliminating the deficiencies noted for the isosceles configuration model. The distribution in parameter *a* that is determined by this fit is shown by curve (*a*) squares in the upper part of Fig. 7. As a check, this *a* distribution was used to generate the synthetic *Z*-ratio spectrum, shown as curve (*c*) in the upper part of Fig. 5. The experimental observation is shown as curve (*d*) in this figure for comparison.

The apparent kinetic-energy release spectrum produced by laser-excitation of the $3d\,^2E''(N=1, G=0, R=1)$ $\nu_0 \leftarrow 2p\,^2A_2''(N=K=0)$ ν_0 transition is presented as spectrum (*a*) in Fig. 6. Acquisition of this spectrum was made with parameters quite different from those employed for the $3s\,^2A_1'$: Only fragments with *Z* not in the intervals $0.4 \leqslant Z \leqslant 0.6$ or $1.67 \leqslant Z \leqslant 2.5$ are accepted, and the set of parameter values ($m_1=1$, $m_2=2$, $M=3$, and $E_0=6$ keV) was used to transform the detected coincidences into an apparent kinetic-energy release histogram with Eq. (2). Apart from the difference in the energy release scale, which is set by these particular mass and energy parameters used for the data acquisition and is not otherwise significant, the spectrum exhibits many of the features seen in the apparent kinetic-energy release spectrum of the $3s\,^2A_1'$ state (Fig. 5). With increasing values of *W*, the signal rises to a local maximum at 2.3 eV, and shows large peaks at 3.5 and 4.0 eV, followed by a sharp cutoff at 4.2 eV. For the Monte Carlo simulation of this spectrum, we assume that the three H atoms are produced with a total kinetic-energy release $W=3.230$ eV by predissociation of the $3d\,^2E''(N=1, G=0, R=1)$ ν_0 level, and that the fragments are ejected in the plane perpendicular to the top axis, whose optical alignment is described by $\beta=0$. Apparent kinetic-energy release distributions, calculated in the simulation at discrete values of parameter *a* and a uniform random distribution of kinematically allowed parameter *b* values, serve as basis functions for fitting the experimental spectrum. A selection of these distributions, cal-

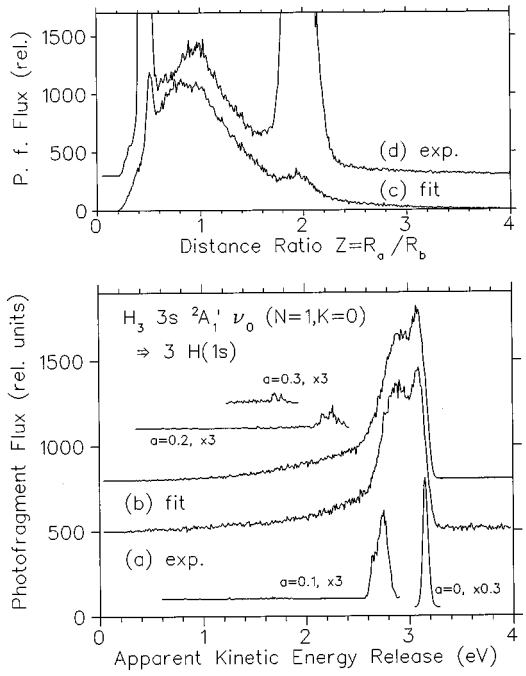

FIG. 6. Lower: Spectrum (*a*): apparent kinetic-energy release following three-body fragmentation of the H_3 $3d\,^2E''(N=1, G=0, R=1)$ initial state. Spectrum (*b*) is a fit to the experimental spectrum by a weighted sum of basis functions. The model used to calculate the basis functions is the same as in Fig. 5. Representative basis functions for $a=0$, 0.1, 0.2, and 0.3 are included in the figure. Note that the energy release scale reflects the choice m_1, m_2, and E_0 used for binning the experimental dissociation events [Eq. (2)], and has no significance either in this figure or in Fig. 5 other than to summarize the correlation between the radial and temporal separations of the dissociation fragments. Upper: Spectrum (*c*): simulation of the apparent *Z*-ratio spectrum using the parameter *a* distribution established for spectrum (*b*). Spectrum (*d*): experimental *Z*-ratio spectrum.

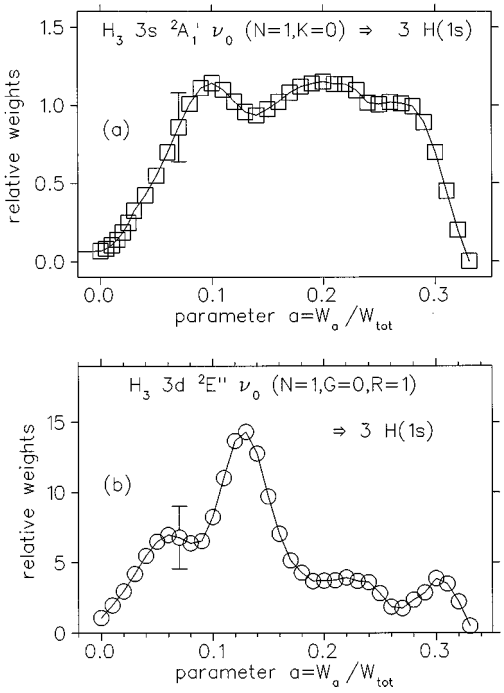

FIG. 7. Distributions of parameter *a* in the unrestricted model required to fit the experimentally observed apparent kinetic energy spectra of the $3s\ ^2A_1'(N=1, K=0)$, curve (*a*) (squares), and the $3d\ ^2E''(N=1, G=0, R=1)$, curve (*b*) (circles), states. Parameter *b* is taken to be uniformly distributed over its allowed range in these fits.

culated for $a=0$, 0.1, 0.2, and 0.3, is presented in Fig. 6 for reference. As was the case for the $3s\ ^2A_1'$ state, the high-energy cutoff in the measured spectrum corresponds to the case of $a=0$, where the total kinetic energy is released into two of the three fragments. Spectrum (*b*) in Fig. 6 is a fit to the measured spectrum by a weighted sum of the basis functions. It can be seen that the fit reproduces all of the features that appear in the measured spectrum. The distribution of parameter *a* basis function contributions determined by the fit is shown by curve (*b*) (circles) in the lower part of Fig. 7. The *Z*-ratio spectrum simulated from this *a* distribution is shown as curve (*c*) in the upper part of Fig. 6. The experimental spectrum is shown as curve (*d*) in this figure for comparison.

IV. DISCUSSION

A. Dissociation configurations

The results of modeling the dissociation fragmentation configurations required to interpret the observed correlations of the H_3 three-body photofragments give some insight into the distortions of nuclear geometry in this symmetric molecule that must accompany predissociation. For the case of the highly restricted isosceles geometry, the fitted *p* distribution shown by curve (*b*) in Fig. 3 shows a very small probability for dissociation in a linear configuration ($p=0$) which increases to a maximum probability in the range of $p=0.4$–0.6, and then decreases for increasing values of *p*. It has previously been noted that in distinguishing between two- and three-body products, we necessarily exclude the detection of three-body products that would have been produced at $p\rightarrow\infty$. However, this does not seriously influence product detection for smaller *p* values, especially in the range $2\leqslant p\leqslant 4$, which appear in Fig. 3. Thus the apparent decrease in the probability of dissociating with configurations described by increasingly large values of the parameter *p* shown by Fig. 3 is presumed to be realistic. In fact, the small probabilities shown for $p=0$ and $p>2$ are not unreasonable, since they represent the limiting cases of imparting all of the released kinetic energy to just two of the three fragments and imparting a maximum amount of released energy to one of the three fragments, respectively. It should be noted that the number of decay processes in which the products are ejected with an equilateral fragmentation geometry ($p=2/\sqrt{3}\cong 1.15$) is also comparatively small, despite the fact that this configuration is consistent with the D_{3h} symmetry of the $3s\ ^2A_1'$ initial state. Rather, the most probable partitioning of velocity to the ejected atoms is intermediate between the linear and equilateral configurations of the isosceles model.

Similar conclusions are reached from the fits to the unrestricted partitioning model. The *a*-parameter distributions (Fig. 7) found for the three-body products of the vibrationless $3s\ ^2A_1'(N=1, K=0)$ and $3d\ ^2E''(N=1, G=0, R=1)$

TABLE I. Branching between three- and two-body dissociation channels in H_3.

Initial H_3 state	Ratio[a]	Source
$3s\ ^2A_1'(N=1,\ K=0)\ \nu_0$	1.44 (1.59)	This work
$3d\ ^2E''(N=1,\ G=0,\ R=1)\ \nu_0$	0.24 (0.51)	This work
$2s\ ^2A_1'$, $2p\ ^2A_2''$ high ν	0.57	DCT, hot ion source, Ref. [7]
$2s\ ^2A_1'$, $2p\ ^2A_2''$	0.23	DCT, cold ion source, Ref. [7]
$2p\ ^2A_2''\ \nu_0$	0.64	Wave-packet theory, Ref. [11]
$3s\ ^2A_1'\ \nu_0$	0.22	Wave-packet theory (NACME), Ref. [2]
$H_3^+ + e^-$ 10 meV	1.3	Dissociative recombination, Ref. [9]
$H_3^+ + e^-$ 1–300 meV	3.0	Dissociative recombination, Ref. [10]

[a]Ratio of the total three- to two-body decay rates. Numbers in parentheses are ratios of the total three and two-body predissociation rates, i.e., excluding the two-body radiative dissociation products.

states both vanish at $a=\frac{1}{3}$, which corresponds to an equilateral geometry, and they are both very small at $a=0$, which corresponds to a collinear geometry. On the other hand, the distributions resulting from the predissociation of these two states show marked differences. In the case of the $3s\ ^2A_1'(N=1,\ K=0)$ state, the distribution between $a=0.1$ and 0.28 is essentially constant, within the statistical uncertainty of the fit, whereas the distribution from the $3d\ ^2E''(N=1,\ G=0,\ R=1)$ state exhibits a narrow maximum centered at $a=0.12$ sitting on a plateau of less probable configurations with $a=0.05-0.3$. A very large difference was also observed in the rovibrational distributions of the H_2 photofragments produced by the two-body predissociation of these two states [6]. As noted there, such large differences in the product distributions cannot reasonably be attributed to the very small difference in energy of these two levels. Rather, they suggest that the nonadiabatic couplings of these states to the ground-state surface [2] must play a major role in their dissociation dynamics.

Although the unrestricted model for the three-body dissociation allows a quite excellent description of the apparent kinetic-energy release distributions produced by predissociation of the $3s\ ^2A_1'$ and $3d\ ^2E''$ states, the corresponding distance ratio distributions are less well explained. In the case of the $3d\ ^2E''$ state, the model Z-ratio distribution peaks more strongly at $Z=1$ than is observed. For the $3s\ ^2A_1'$ state, the model yields somewhat fewer events in the region of $Z=1$ than observed. In neither case are the discrepancies large, but no variations in the parameter a basis function distributions were able to remove them while retaining a good description of the apparent kinetic-energy release distributions. It is likely that choosing a parameter b distribution other than uniform or explicitly fitting the parameter b distributions would eliminate such discrepancies, but we have chosen not to attempt this here.

B. Branching ratios

The Monte Carlo simulation allows us to establish the relative collection efficiencies of the detector for two- and three-body fragments. Using these efficiencies and the measured fluxes of three- and two-body dissociation products from the H_3 $3s\ ^2A_1'$ and $3d\ ^2E''$ states, we can estimate the relative contributions of three- and two-body [6] decay processes to the dissociation of these states. These branching ratios are given in Table I using the unrestricted fragmentation geometry model for the three-body collection efficiencies. As a measure of the sensitivity of these ratios to the three-body fragmentation model, we note that the three-/two-body decay ratio that is predicted using the collection efficiency from the isosceles model (3.2) is roughly a factor of 2 larger than the ratio derived from the unrestricted model, which should be preferred.

The three-/two-body ratio of the $3s\ ^2A_1'$ state is found to be a factor of 9 higher than for the $3d\ ^2E''$ state, although the energies of these two states above the three-body dissociation limit differ by only about 3%. This large difference in the relative three-body dissociation rates for these two states is consistent with that implied by a comparison of the theoretical transition rates and measured lifetimes of these two states [6].

We can combine the present measurements of the three-/two-body ratios with our previous determination [6] of the branching ratios between the two-body predissociation and (two-body) radiative decay to the ground state surface. The results, listed in Table II, define the complete distribution of dissociation products for the $3s\ ^2A_1'$ and $3d\ ^2E''$ levels. As already deduced from a comparison between the lifetime and the radiative transition rate [6], three-body decay turns out to be the dominant fragmentation process of the $3s\ ^2A_1'$ state. The main decay process of the $3d\ ^2E''$ state is a radiative transition onto the lower sheet of the repulsive ground-state surface, which leads to production of $H+H_2$.

Peterson *et al.* [7] measured three-/two-body ratios of the $n=2$ states of H_3 prepared by charge transfer in cesium. The ratio was found to increase with the vibrational excitation of the initial state. Peterson *et al.* [7] reported values of 0.23 for a cold rovibrational distribution and 0.57 for a hot distribution. The ratio of the $n=2$ state at low vibrational excitation is in excellent agreement with our result for the $3d\ ^2E''$ state. Quite high three/two-body ratios were observed in investigations of the dissociative recombination of H_3^+ molecules with free electrons. Mitchell [9] found a three- to two-body branching of 1.3 from dissociative recombination of H_3^+. A branching ratio of about 3.0 was observed for this reaction by Datz *et al.* [10]. Very high-n Rydberg states of H_3 are believed to be involved in the dynamics of the dissociative recombination process [9]. The general trend seems to be an increase in the three-/two-body ratio with increasing vibrational and electronic excitation energy of the H_3 state, as suggested earlier by Peterson *et al.* [7]. On the other hand,

TABLE II. Partitioning among the decay channels of radiative dissociation, two-body predissociation, and three-body predissociation decay channels for the ground vibrational levels in the $3s\ ^2A_1'$ and $3d\ ^2E''$ states of H_3.

H_3 state	Two-body (H+H_2)		Three-body (H+H+H)
	Radiative	Predissociation	Predissociation
$3s\ ^2A_1'(N=1,\ K=0)\ \nu_0$	4%	37%	59%
$3d\ ^2E''(N=1,\ G=0,\ R=1)\ \nu_0$	49%	32%	19%

the huge difference in branching ratio observed here for the $3s\ ^2A_1'$ and $3d\ ^2E''$ states, which are nearly degenerate in energy, clearly demonstrates that the specific dissociation dynamics of an H_3 state ultimately controls the distribution of its products among the open dissociation channels.

The results of the theoretical investigations by Orel and Kulander [11] and by Krause *et al.* [2] do not include the contribution from the radiative decay to the ground-state surface in their branching ratios. Therefore, we also list the ratios of the total three-body rate to the two-body predissociation rate, given in parentheses in Table I. The calculations of Orel and Kulander [11] for the vibrationless $2p\ ^2A_2''$ state are in excellent agreement with our value for the $3d\ ^2E''$ state. On the other hand, inclusion of nonadiabatic coupling matrix elements by Krause *et al.* [2] led to a quite small three-/two-body branching ratio of 0.22 which is by a factor of about 2.5 smaller than the experimental value of the $3d\ ^2E''$ state and about a factor of about 7 smaller than that of the $3s\ ^2A_1'$ state. One reason for the large discrepancy might be that our laser-prepared H_3 states have one quantum of rotational excitation, whereas none of the theoretical calculations consider the effects of rotation. The $3d\ ^2E''$ state is coupled to the repulsive ground-state surface by rotation about an axis perpendicular to the top axis [20]. In contrast, the $3s\ ^2A_1'$ state is coupled by a degenerate mode vibration to the ground-state surface [21]. This difference in coupling mechanisms might explain the large observed difference of the three-/two-body ratios between the $3s\ ^2A_1'$ and the $3d\ ^2E''$ initial states. Only the nonadiabatic coupling due to vibrational motion was taken into account in the theoretical investigation by Krause *et al.* [2]. It is therefore ironic that their theoretical value is quite close to the experimental value for the $3d\ ^2E''$ state which is not subject to vibrational predissociation.

A second reason for the relatively large yield of H+H+H in the dissociation of the $3s\ ^2A_1'$ state may be found in the possibility of a homogeneous perturbation by the upper sheet of the ground-state surface, which adiabatically correlates to that limit. Petsalakis, Theodorakopoulos, and Wright [22] calculated that, in collinear geometry, the $2p\ 1\ ^2\Sigma_g^+$ upper sheet of the ground-state surface undergoes a series of avoided crossings with the manifold of higher-energy states with $^2\Sigma_g^+$ symmetry [21]. These include the $2s\ ^2A_1'$ ($2\ ^2\Sigma_g^+$) and $3s\ ^2A_1'$ states, but not the $3d\ ^2E''$ state. The $2s\ ^2A_1'$ state is known to undergo strong predissociation, though its products are predominantly H+H_2 [6], presumably because of efficient coupling between the upper and lower sheets of the ground-state surface during the course of the dissociation. For this process to account effectively for a high three-body yield from the higher energy $3s\ ^2A_1'$ state, the shorter interaction time allowed by the much higher kinetic energy of its separating atoms would have to effectively minimize coupling to the lower sheet of the ground-state surface.

V. CONCLUSIONS

H_3 molecules, selectively prepared in the $3s\ ^2A_1'(N=1,\ K=0)\ \nu_0$ and $3d\ ^2E''(N=1,\ G=0,\ R=1)\ \nu_0$ levels by laser excitation, are observed to predissociate into both the H+H_2 and H+H+H dissociation channels. This latter, three-body dissociation channel was examined by detecting two of the three fragments and measuring their radial and temporal separations. Although the present experiment allowed the H+H+H channel to be examined without interference from other dissociation products, the present detector geometry was not suitable for determining the individual velocity vectors of the H-atom products. However, by mathematically describing the detector response to all possible configurations of the product velocities, Monte Carlo trajectory simulations could be used to reproduce the observed radial and temporal separations of the detected products. Parametrizing the kinematic relationships among the H-atom velocities and utilizing the well-defined total energies released by the dissociation of the two discrete H_3 levels allowed the specific classes of geometries for the three H atoms to be determined for each level using Monte Carlo simulations. In addition, the simulations allowed the flux of the three-body dissociation products to be determined relative to the flux of two-body fragments.

The remarkable finding here is that the products from predissociation of the $3s\ ^2A_1'$ and $3d\ ^2E''$ levels are so completely different. Only 19% of the $3d\ ^2E''$ state's products go into the H+H+H channel, and this dissociation proceeds through only a relatively narrow range of nuclear configurations, i.e., the distribution of parameter a in the unrestricted model has a narrow peak. In contrast, H+H+H accounts for 59% of the $3s\ ^2A_1'$ state's products, and these are produced from a wide variety of nuclear configurations, as evidenced by the broad distribution of parameter a. Although previous observations of three-body dissociation have consistently indicated that this process becomes more facile as the total energy in the H_3 increases, such a trend is contraindicated here by the clear difference in behavior of the $3s\ ^2A_1'$ and $3d\ ^2E''$ states. Since both of these levels lie within a few percent of each other in total energy above the ground-state potential surface, the total energy can hardly play a determining role in their dissociation dynamics. On the other hand, the predissociation mechanisms of these two states are quite different. The $3s\ ^2A_1'$ state is predissociated to the ground-state continuum by vibrational coupling along the de-

generate (bending) mode, whereas the $3d\,^2E''$ state is coupled by rotation.

We note that the present modeling of the three-body kinematics is limited by the fact that we have assumed a uniform distribution in parameter b of the unrestricted model because of the severe limitations of the present detector, which measures the radial and temporal separations of only two of the three fragments. A significant improvement would be made if the full set of Cartesian coordinates for each of the three fragments were explicitly determined by the detector.

ACKNOWLEDGMENTS

This work was partially supported by the National Science Foundation under Grant No. PHY-9111872. One of us (U.M.) gratefully acknowledges support from the Deutsche Forschungsgemeinshaft. We acknowledge very useful discussions with Dr. H. Helm and Dr. D. L. Huestis during the course of this work. We gratefully acknowledge the skilled assistance of Alina Dykman, who participated in this work under the Research Experience for Undergraduates Program for the National Science Foundation, supported by Grant No. PHY-93000247.

[1] Ch. Nager and M. Jungen, Chem. Phys. **70**, 189 (1982).
[2] J. L. Krause, A. E. Orel, B. H. Lengsfield, and K. C. Kulander, in *Time-Dependent Quantum Molecular Dynamics*, edited by J. Broeckhove and L. Lathouwers (Plenum, New York, 1992), p. 131.
[3] D. Azinovic, R. Bruckmeier, Ch. Wunderlich, and H. Figger, Phys. Rev. A **58**, 1115 (1998).
[4] S. Mahapatra and H. Köppel, J. Chem. Phys. **109**, 1721 (1998).
[5] S. Mahapatra and H. Köppel, Phys. Rev. Lett. **81**, 3116 (1998).
[6] U. Müller and P. C. Cosby, J. Chem. Phys. **105**, 3532 (1996).
[7] J. R. Peterson, P. Devynck, Ch. Hetzler, and W. G. Graham, J. Chem. Phys. **96**, 8128 (1992).
[8] J. B. A. Mitchell, J. L. Forand, C. T. Ng, D. P. Levac, R. E. Mitchell, P. M. Mul, W. Claeys, A. Sen, and J. W. McGowan, Phys. Rev. Lett. **51**, 885 (1983).
[9] J. B. A. Mitchell, Phys. Rep. **186**, 215 (1990).
[10] S. Datz, G. Sundström, Ch. Biedermann, L. Broström, H. Danared, S. Mannervik, J. R. Mowat, and M. Larsson, Phys. Rev. Lett. **74**, 896 (1995).
[11] A. E. Orel and K. C. Kulander, J. Chem. Phys. **91**, 6086 (1989).
[12] H. Helm and P. C. Cosby, J. Chem. Phys. **86**, 6813 (1987).
[13] C. Bordas, P. C. Cosby, and H. Helm, J. Chem. Phys. **93**, 6303 (1990).
[14] D. P. de Bruijn and J. Los, Rev. Sci. Instrum. **53**, 1020 (1982).
[15] R. N. Zare, Ber. Bunsenges. Phys. Chem. **86**, 422 (1982).
[16] The $3d\,^2E''(N=1, G=0, R=1)$ level can be described in terms of two Hund's case d basis functions with $(N^+=1, K^+=0)$ and $(N^+=3, K^+=0)$ core rotational excitation, respectively (Ref. [17]). However, analysis of the analogous f Rydberg series has found the $(N^+=3, K^+=0)$ component to contribute less than $\sqrt{0.073}$ to the total amplitude of the state (Ref. [17]); therefore, we neglect it here. For an $N=1$, $L=2$, $M=0$ state built on a pure $(N^+=1, K^+=0)$ core, we calculate an asymmetry parameter $\beta=0.2$ to describe the alignment of the H_3^+ core top axis.
[17] L. J. Lembo, M. C. Bordas, and H. Helm, Phys. Rev. A **42**, 6660 (1990).
[18] J. L. Krause, K. C. Kulander, J. C. Light, and A. E. Orel, J. Chem. Phys. **96**, 4283 (1992).
[19] P. C. Cosby and H. Helm, Chem. Phys. Lett. **152**, 71 (1988).
[20] I. Dabrowski and G. Herzberg, Can. J. Phys. **58**, 1238 (1980).
[21] H. Helm, in *Dissociative Recombination*, edited by B. R. Rowe, J. B. A. Mitchell, and A. Canosa (Plenum, New York, 1993), p. 145.
[22] I. D. Petsalakis, G. Theodorakopoulos, and J. S. Wright, J. Chem. Phys. **89**, 6850 (1988).